

Dynamic Differential Linear Attention: Enhancing Linear Diffusion Transformer for High-Quality Image Generation

Boyuan Cao^{1*} XingBo Yao^{2*} Chenhui Wang¹ Jixin Ye¹ Yujie Wei¹ Hongming Shan^{1†}

¹Fudan University ²Hong Kong University of Science and Technology (Guangzhou)

{caoby23, chenhuiwang21, jxye22, yjwei22}@m.fudan.edu.cn, hmshan@fudan.edu.cn
xyao739@connect.hkust-gz.edu.cn

Abstract

Diffusion transformers (DiTs) have emerged as a powerful architecture for high-fidelity image generation, yet the quadratic cost of self-attention poses a major scalability bottleneck. To address this, linear attention mechanisms have been adopted to reduce computational cost; unfortunately, the resulting linear diffusion transformers (LiTs) models often come at the expense of generative performance, frequently producing over-smoothed attention weights that limit expressiveness. In this work, we introduce Dynamic Differential Linear Attention (DyDiLA), a novel linear attention formulation that enhances the effectiveness of LiTs by mitigating the oversmoothing issue and improving generation quality. Specifically, the novelty of DyDiLA lies in three key designs: (i) dynamic projection module, which facilitates the decoupling of token representations by learning with dynamically assigned knowledge; (ii) dynamic measure kernel, which provides a better similarity measurement to capture fine-grained semantic distinctions between tokens by dynamically assigning kernel functions for token processing; and (iii) token differential operator, which enables more robust query-to-key retrieval by calculating the differences between the tokens and their corresponding information redundancy produced by dynamic measure kernel. To capitalize on DyDiLA, we introduce a refined LiT, termed DyDi-LiT, that systematically incorporates our advancements. Extensive experiments show that DyDi-LiT consistently outperforms current state-of-the-art (SOTA) models across multiple metrics, underscoring its strong practical potential.

1. Introduction

Diffusion Transformers (DiTs) have shown remarkable performance in image and video generation [4, 8, 22, 27, 35, 38]. Despite their promise, DiTs incur quadratic computational complexity with respect to (w.r.t.) sequence length due to

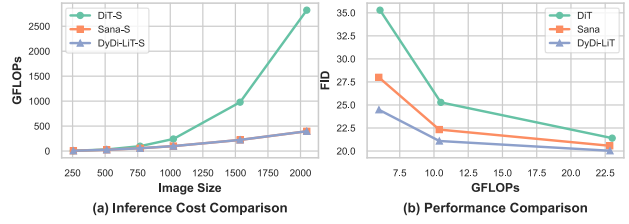


Figure 1. **Inference cost and performance comparisons** among DiT [27] using Softmax attention, Sana [41] using linear attention, and our DyDi-LiT using DyDiLA. DyDiLA achieves SOTA performance with negligible additional computational overhead.

self-attention, making high-resolution synthesis prohibitively expensive, as shown in Fig. 1(a).

To mitigate this problem, many studies introduce more efficient architectures that *either* compress the information involved in attention calculation [1, 3, 18, 29] or substitute Transformers with classical sequential models [9, 17, 44, 47]. However, compressing information within attention risks discarding salient information [12, 39, 40], and sequential substitutes lack global modeling capacity [46], ultimately constraining the achievable generation quality. More recently, replacing Softmax attention in DiTs with linear attention has produced Linear Diffusion Transformers (LiTs), which currently set the benchmark [1, 21, 36, 41, 42].

However, existing LiTs rely on unmodified linear attention, whose low-variance, over-smoothed attention weights obscure fine-grained token distinctions and ultimately degrade image quality [13, 37]. We attribute this over-smoothing effect to *token heterogeneity*, *suboptimal similarity measurement*, and *context-sensitive retrieval*. First, tokens arising from different denoising time-steps and spatial positions exhibit heterogeneous distributions [10, 34, 43], and mapping them indiscriminately into a shared representation space neglects these variations, leading to homogenized token representations and degrades matching accuracy. Second, vanilla linear attention measures similarity by applying rectified linear unit (ReLU)-activated Q and K matrices, but without the exponential scaling in Softmax operation, it fails to capture fine-grained semantic distinctions between

*Equal contribution

†Corresponding author

tokens [12, 33]. Third, conventional query-to-key retrieval paradigm shows sensitivity to context tokens due to redundant information in tokens, frequently leading to overallocated attention weights to many semantically irrelevant key tokens, resulting in inferior context aggregation [24, 45].

To alleviate these issues, we propose dynamic differential linear attention, termed DyDiLA, which delivers better generation results while remaining linear computational complexity. DyDiLA mitigates the aforementioned three issues through three architectural designs: **(i)** dynamic projection module, which facilitates more disentangled token representations by projecting tokens using dynamically assigned knowledge; **(ii)** dynamic measure kernel, which more accurately measures the semantic similarity between the tokens through processing tokens using dynamically designated kernel functions; and **(iii)** token differential operator, which enhances the robustness of query-to-key retrieval by computing the differences between tokens and their corresponding information redundancy produced by dynamic measure kernel. Building on DyDiLA, we further introduce an enhanced LiT architecture, termed DyDi-LiT. Fig. 1(b) shows that DyDiLA unlocks LiTs with negligible extra computational overhead, highlighting its potential to generate higher-resolution images with superior quality.

Our contributions are summarized as follows.

- We propose dynamic differential linear attention, a novel attention mechanism that enhances the effectiveness of linear diffusion transformers, unlocking their potential to generate high-quality images.
- We propose dynamic projection module to promote token representation disentanglement for better token matching.
- We propose dynamic measure kernel to better measure the similarity between tokens for capturing fine-grained semantic differences.
- We propose token differential operator, which provides robust query-to-key retrieval for better context aggregation.
- To exploit the full potential of DyDiLA, we further introduce DyDi-LiT. Extensive experiments demonstrate that DyDi-LiT significantly outperforms the vanilla DiT model and SOTA efficient diffusion models.

2. Related Work

Prior research on efficient DiT architectures falls into three main categories: attention compression, sequential modeling, and linear attention. We subsequently introduce each.

Attention compression-based methods. The main idea of this line of research is to prune attention components (*e.g.*, tokens or attention heads) to reduce computational overhead. Token pruning either replaces the original query and key tokens with a compact set of agent tokens through cross attention [29] or directly compresses them using convolutional or pooling operations [1, 3]. Attention head pruning, on the other hand, routes a key subset of attention heads for cal-

culation [18]. Although computationally efficient, attention compression is prone to discard salient features and thus impair generative quality [12, 13, 39, 40].

Sequential model-based methods. These methods replace the Transformer architecture with classical sequential models, *e.g.* Mamba [11], reducing computational complexity to $\mathcal{O}(N)$ [9, 17, 44, 47]. Despite this efficiency, they rely on intricate scanning strategies and inevitably sacrifices long-range modeling capabilities. A recent study [46] suggests that Mamba-like architectures are better suited for tasks requiring causal token mixing, indicating that sequential models may not be the optimal choice for image generation.

Linear attention-based methods. These methods replace Softmax attention with linear alternatives, reducing computational complexity to $\mathcal{O}(N)$ [1, 21]. Recent work, exemplified by Sana [41], reports impressive performance. Nonetheless, linear attention mechanisms have yet to fully realize their potential due to suboptimal architectural designs. To offset this gap, some studies employ DiT-based distillation [36] or inference scaling [42] to further enhance performance. In contrast, we aim at designing an optimized architecture to unlock the full generative potential of linear attention.

3. Method

DyDi-LiT. Fig. 2(a) presents the overview of DyDi-LiT. The DyDi-LiT comprises L blocks for conditional information injection. The input noise latent tokens are obtained through variational auto encoder (VAE) [19] tokenization and forward diffusion, while the timestep and class-conditional information are injected via adaptive layer normalization (AdaLN) [28].

3.1. Dynamic Differential Linear Attention

The dynamic differential linear attention (DyDiLA) consists of three components: dynamic projection module, dynamic measure kernel, and token differential operator, as shown in Fig. 2(b). For the input token matrix \mathbf{X} , dynamic projection module first employs token-shared projectors to obtain \mathbf{Q} , \mathbf{K} , and \mathbf{V} , while simultaneously using token-specific projectors to transform each token into decoupled representations \mathbf{Q}' and \mathbf{K}' , which are considered as redundancy information. Next, dynamic measure kernel assigns a dedicated kernel function to each token in \mathbf{Q} , \mathbf{K} , \mathbf{Q}' and \mathbf{K}' , producing $\widetilde{\mathbf{Q}}$, $\widetilde{\mathbf{K}}$, $\widetilde{\mathbf{Q}}'$, and $\widetilde{\mathbf{K}}'$, enabling better similarity measurement. Finally, token differential operator applies token-specific scaling factors to compute the differences of the matrix pairs $(\widetilde{\mathbf{Q}}, \widetilde{\mathbf{Q}}')$ and $(\widetilde{\mathbf{K}}, \widetilde{\mathbf{K}}')$ and uses these differences to calculate the attention output. Next, we detail each key components.

Dynamic projection module. To promote token representation disentanglement, we propose dynamic projection module, which dynamically projects each token using a projector possessing distinct knowledge. Similar to vanilla Soft-

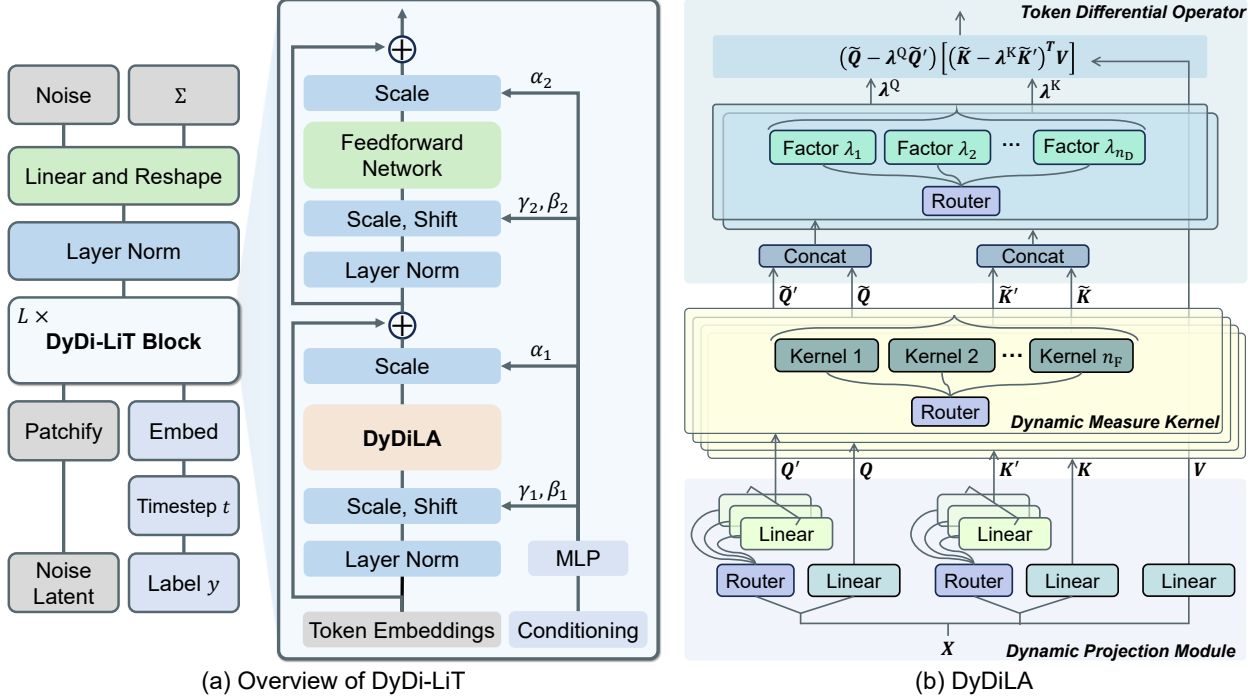


Figure 2. **Overview of DyDi-LiT.** (a) DyDi-LiT comprises L blocks that receive noise tokens encoded by VAE, and AdaLN injects timestep and class information into every block. (b) DyDiLA comprises three components—dynamic projection module, dynamic measure kernel, and token differential operator—responsible respectively for disentangling token representations, providing more accurate token similarity measurement, and strengthening query-key retrieval robustness.

max attention in DiT, dynamic projection module first obtain the \mathbf{Q} , \mathbf{K} , and \mathbf{V} matrices using three token-shared projectors: $[\mathbf{Q}, \mathbf{K}, \mathbf{V}] = [\mathbf{X} \mathbf{W}_0^Q, \mathbf{X} \mathbf{W}_0^K, \mathbf{X} \mathbf{W}_0^V]$, where $\mathbf{X} \in \mathbb{R}^{N \times d}$, $\mathbf{W}_0 \in \mathbb{R}^{d \times d}$, and N and d are the number of tokens and token dimension, respectively. Different from DiT, dynamic projection module additionally predicts the information redundancy components \mathbf{Q}' and \mathbf{K}' for \mathbf{Q} and \mathbf{K} . Each token in \mathbf{Q}' and \mathbf{K}' is obtained using a token-specific projector. Specifically, dynamic projection module first defines two sets of projectors for \mathbf{Q}' and \mathbf{K}' : $\{\mathbf{W}_i^Q \in \mathbb{R}^{d \times d} \mid i = 1, \dots, n_P\}$ and $\{\mathbf{W}_i^K \in \mathbb{R}^{d \times d} \mid i = 1, \dots, n_P\}$, where n_P is the number of projectors. Then, dynamic projection module routes each token $\mathbf{X}_i \in \mathbb{R}^{1 \times d}$ ($i = 1, \dots, N$) in \mathbf{X} to its respective \mathbf{Q}' and \mathbf{K}' projectors:

$$u_i = \arg \max_{u \in \{1, \dots, n_P\}} (\mathbf{X}_i \mathbf{R}_P^Q)_u, \quad v_i = \arg \max_{v \in \{1, \dots, n_P\}} (\mathbf{X}_i \mathbf{R}_P^K)_v, \quad (1)$$

where u_i and v_i are the indices of the selected projectors for the i -th token \mathbf{X}_i , and $\mathbf{R}_P^Q, \mathbf{R}_P^K \in \mathbb{R}^{d \times n_P}$ are the routers for \mathbf{Q}' and \mathbf{K}' , respectively. Finally, \mathbf{Q}'_i and \mathbf{K}'_i are calculated by applying the selected projectors to \mathbf{x}_i :

$$[\mathbf{Q}'_i, \mathbf{K}'_i] = [\mathbf{X}_i \mathbf{W}_{u_i}^Q, \mathbf{X}_i \mathbf{W}_{v_i}^K]. \quad (2)$$

Then, \mathbf{Q} , \mathbf{K} , \mathbf{Q}' , and \mathbf{K}' are fed into dynamic measure kernel module, where they are processed using kernel functions.

Dynamic measure kernel. To provide a better similarity measurement for capturing fine-grained semantic differences

between tokens, we propose dynamic measure kernel. For better illustrating this module, let us begin with the standard Softmax attention used in DiT [27]. Considering a single-head setting for simplicity, given $\mathbf{Q}, \mathbf{K}, \mathbf{V} \in \mathbb{R}^{N \times d}$, Softmax attention can be expressed as:

$$\mathbf{O}_i = \sum_{j=1}^N \frac{\text{Sim}(\mathbf{Q}_i, \mathbf{K}_j)}{\sum_{m=1}^N \text{Sim}(\mathbf{Q}_i, \mathbf{K}_m)} \mathbf{V}_j, \quad (3)$$

where $\mathbf{Q}_i, \mathbf{K}_i, \mathbf{V}_i \in \mathbb{R}^{1 \times d}$, and $\text{Sim}(\cdot, \cdot) = \exp(\mathbf{Q}_i \mathbf{K}_i^T / \sqrt{d})$. In contrast, linear attention replaces the exponential similarity with a kernel function $\phi(\cdot)$, i.e. $\text{Sim}(\mathbf{Q}_i, \mathbf{K}_i) = \phi(\mathbf{Q}_i) \phi(\mathbf{K}_i)^T$, enabling the computation to first multiply $\phi(\mathbf{K})^T$ and \mathbf{V} , which results in a more efficient formulation. In this case, Eq. (3) can be reformulated as:

$$\mathbf{O}_i = \frac{\phi(\mathbf{Q}_i) \left(\sum_{j=1}^N \phi(\mathbf{K}_j)^T \mathbf{V}_j \right)}{\phi(\mathbf{Q}_i) \left(\sum_{m=1}^N \phi(\mathbf{K}_m)^T \right)} \quad (4)$$

In this manner, we change the computational order from $(\mathbf{Q} \mathbf{K}^T) \mathbf{V}$ to $\mathbf{Q} (\mathbf{K}^T \mathbf{V})$; thus the computation complexity w.r.t. the number of token is optimized to $\mathcal{O}(N)$.

The core idea of dynamic measure kernel is to adjust token directions adaptively while preserving their norms, thereby amplifying the dot products among semantically related tokens. Inspired by [12], which showed that norm-preserving power operations cluster semantically similar

tokens, we formalize this process as:

$$\tilde{\mathbf{Z}}_i = \phi(\mathbf{Z}_i) = \frac{\text{ReLU}(\mathbf{Z}_i)^\gamma}{\|\text{ReLU}(\mathbf{Z}_i)^\gamma\|_2} \cdot \|\text{ReLU}(\mathbf{Z}_i)\|_2, \quad (5)$$

where $\mathbf{Z} \in \mathbb{R}^{N \times d}$ is the input token matrix with $\mathbf{Z}_i \in \mathbb{R}^{1 \times d}$ for $i = 1, \dots, N$, and γ is a scalar kernel hyperparameter.

However, Eq. (5) employs an identical γ to adjust the directions of all tokens, disregarding the heterogeneity in token information. By contrast, dynamic measure kernel remedies this limitation by assigning token-specific, norm-preserving kernel functions to improve similarity estimation. Considering the importance of initializing γ [12], we initialize a set of learnable kernel factors: $\{\gamma_1, \dots, \gamma_{n_F}\}$, where n_F denotes the number of factors. In this way, we simultaneously define a set of routable kernel functions $\{\phi_1, \dots, \phi_{n_F}\}$. Accordingly, each token \mathbf{Z}_i is routed to a specific kernel function to enhance focus, formulated as:

$$\tilde{\mathbf{Z}}_i = \phi_{f_i^Z}(\mathbf{Z}_i), \text{ where } f_i^Z = \arg \max_{f \in \{1, \dots, n_F\}} (\mathbf{Z}_i \mathbf{R}_F^Z)_f. \quad (6)$$

Here, f_i^Z is the index of the selected kernel for the i -th token of \mathbf{Z} , $\mathbf{R}_F^Z \in \mathbb{R}^{d \times n_F}$ denotes the router matrix for the token matrix \mathbf{Z} , and (\cdot) represents tokens processed by kernel functions. In practice, $\mathbf{Z} \in \{\mathbf{Q}, \mathbf{K}, \mathbf{Q}', \mathbf{K}'\}$. Then, \mathbf{Q} , \mathbf{K} , \mathbf{Q}' , and \mathbf{K}' are processed by dynamic measure kernel to obtain $\tilde{\mathbf{Q}}$, $\tilde{\mathbf{K}}$, $\tilde{\mathbf{Q}'}$, and $\tilde{\mathbf{K}'}$, which are then fed into token differential operator for differential computation.

Token differential operator. To promote more robust query-to-key retrieval, we propose token differential operator (TDO), which calculates the differences between the tokens and their corresponding information redundancy produced by dynamic measure kernel. Specifically, token differential operator first defines a set of learnable differential factors: $\{\lambda_1, \dots, \lambda_{n_D}\}$, where n_D is the number of learnable factors. Then, it concatenates the token pairs $(\tilde{\mathbf{Q}}, \tilde{\mathbf{Q}'})$ and $(\tilde{\mathbf{K}}, \tilde{\mathbf{K}'})$ to obtain $\tilde{\mathbf{Q}}^C = \text{concat}(\tilde{\mathbf{Q}}, \tilde{\mathbf{Q}'})$ and $\tilde{\mathbf{K}}^C = \text{concat}(\tilde{\mathbf{K}}, \tilde{\mathbf{K}'})$, where $\tilde{\mathbf{Q}}^C, \tilde{\mathbf{K}}^C \in \mathbb{R}^{N \times 2d}$. Subsequently, two distinct routers are used to select token-wise λ for $\tilde{\mathbf{Q}}^C$ and $\tilde{\mathbf{K}}^C$. Specifically, for $\tilde{\mathbf{Q}}_i^C, \tilde{\mathbf{K}}_i^C \in \mathbb{R}^{1 \times 2d}$ ($i = 1, \dots, N$), we compute:

$$l_i^Q = \arg \max_{l \in \{1, \dots, n_D\}} (\tilde{\mathbf{Q}}_i^C \mathbf{R}_D^Q)_l, \quad l_i^K = \arg \max_{l \in \{1, \dots, n_D\}} (\tilde{\mathbf{K}}_i^C \mathbf{R}_D^K)_l, \quad (7)$$

where l_i^Q and l_i^K are the indices for the selected differential factors, and $\mathbf{R}_D^Q, \mathbf{R}_D^K \in \mathbb{R}^{2d \times n_D}$ are the routers for $\tilde{\mathbf{Q}}^C$ and $\tilde{\mathbf{K}}^C$. In this way, we obtain two sets of differential factors for query and key, denoted as: $\boldsymbol{\lambda}^Q = [\lambda_{l_1^Q}; \dots; \lambda_{l_N^Q}]$ and $\boldsymbol{\lambda}^K = [\lambda_{l_1^K}; \dots; \lambda_{l_N^K}]$, where $\boldsymbol{\lambda}^Q, \boldsymbol{\lambda}^K \in \mathbb{R}^{N \times 1}$. Finally, using the routed, token-specific differential factors, we compute token differences, thereby yielding distengled tokens

for subsequent attention:

$$\begin{aligned} \text{TDO}(\tilde{\mathbf{Q}}, \tilde{\mathbf{Q}'}, \tilde{\mathbf{K}}, \tilde{\mathbf{K}'}, \mathbf{V}) \\ = (\tilde{\mathbf{Q}} - \boldsymbol{\lambda}^Q \tilde{\mathbf{Q}'}) \left((\tilde{\mathbf{K}} - \boldsymbol{\lambda}^K \tilde{\mathbf{K}'})^T \mathbf{V} \right), \end{aligned} \quad (8)$$

3.2. Dynamic Differential Linear Attention Module

Based on the aforementioned analysis, we propose a novel linear attention module, dubbed dynamic differential linear attention, which retains linear computational complexity while delivering better generation performance. Inspired by [7, 12], we adopt re-parameterized 3×3 depth-wise convolutions to further enrich the diversity of features in linear attention. Thus, the output of DyDiLA can be formulated as:

$$\mathbf{O} = \text{TDO}(\cdot) + \text{DWC}(\mathbf{V}), \quad (9)$$

where $\text{DWC}(\cdot)$ denotes the depth-wise convolutions.

We notice a recent study [45] suggests that computing differences between attention maps can enhance self-attention's query-to-key retrieval ability and improve the performance on natural language processing tasks. We wonder whether token-wise and attention map-wise differential computations yield similar effects. To explore this, in our ablation experiments, we replace the token-wise differential in Eq. (8) with an attention map-wise differential paradigm, yielding:

$$\mathbf{O} = \tilde{\mathbf{Q}}(\tilde{\mathbf{K}}^T \mathbf{V}) - \boldsymbol{\lambda}_{\text{map}} \tilde{\mathbf{Q}'}(\tilde{\mathbf{K}'}^T \mathbf{V}) + \text{DWC}(\mathbf{V}), \quad (10)$$

where $\boldsymbol{\lambda}_{\text{map}}$ is obtained similar to Eq. (7).

4. Experiments

4.1. Experimental Settings

Benchmarks and implementation details. We conduct experiments at both 256×256 and 512×512 resolutions, training three model variants (small, base, and large) for each architecture. Our experiments are conducted using four NVIDIA 3090 GPUs. Due to limited computational resources, our experiments are performed on ImageNet-1K [31] and its subsets (Sub-IN). Specifically, on ImageNet-1K, we train the small variants at a resolution of 256×256 for standard comparison with recent SOTA models, while all other experiments are conducted on Sub-IN. On ImageNet-1K, we mirror the original DiT [27] configurations: a 256 batch size, 400K training iterations, an AdamW optimizer [6, 23] without weight decay, a 1e-4 learning rate, and a 0.9999 exponential moving average (EMA) decay rate. Following DiT [27], the only data augmentation we use is horizontal flips. All diffusion-related settings remain consistent with those in DiT [27]. Specifically, we use 1000 diffusion steps with a linear variance schedule ranging from 1×10^{-4} to 2×10^{-2} (i.e., the same hyper-parameters from ADM [5]). The pre-trained VAE model [19] used is also taken from Stable Diffusion [30].

Models	CFG=1.0							CFG=4.0							GFLOPs
	FID ↓	sFID ↓	KID ↓	sKID ↓	IS ↑	P% ↑	R% ↑	FID ↓	sFID ↓	KID ↓	sKID ↓	IS ↑	P% ↑	R% ↑	
DiT-S [27]	111.85	11.81	0.0931	0.0053	13.77	20.50	43.54	35.29	7.15	0.0080	0.0010	43.28	47.05	28.23	6.06
DiG-S [47]	129.04	14.61	0.1071	0.0075	11.79	19.68	34.17	44.83	7.68	0.0129	0.0014	37.73	42.90	25.01	5.92
PixArt- Σ -S [3]	121.15	14.62	0.0991	0.0072	12.30	18.50	35.90	40.74	7.70	0.0103	0.0012	40.35	42.44	27.82	5.78
EDiT [1]	118.46	12.20	0.0935	0.0055	13.14	18.63	35.37	37.40	8.15	0.0083	0.0016	43.34	46.92	21.05	5.91
Sana-S [41]	103.74	10.69	0.0833	0.0046	15.81	22.40	45.13	28.00	6.95	0.0044	0.0011	49.37	55.01	22.61	5.97
DyDi-LiT-S	94.08	9.95	0.0727	0.0043	17.42	24.69	50.75	24.48	6.49	0.0033	0.0009	53.82	63.26	20.93	5.98
DiT-B [27]	96.66	9.50	0.0798	0.0040	16.61	24.69	52.37	25.28	6.70	0.0038	0.0009	51.06	57.74	24.07	10.50
DiG-B [47]	122.74	12.49	0.0995	0.0060	12.49	20.17	34.18	43.33	8.02	0.0112	0.0015	38.67	40.87	22.68	10.43
PixArt- Σ -B [3]	107.98	12.10	0.0880	0.0056	14.48	21.71	42.33	30.96	7.10	0.0057	0.0011	47.35	53.23	24.48	10.13
EDiT [1]	103.48	9.80	0.0806	0.0039	15.82	21.70	44.44	29.04	7.66	0.0046	0.0014	50.59	56.02	20.95	10.45
Sana-B [41]	88.65	8.80	0.0696	0.0035	18.77	27.05	49.69	22.33	6.55	0.0031	0.0010	56.76	65.08	21.42	10.38
DyDi-LiT-B	79.84	8.25	0.0602	0.0033	20.93	30.15	53.17	21.09	6.29	0.0036	0.0009	59.94	72.26	19.77	10.39
DiT-L [27]	77.32	7.49	0.0613	0.0027	21.45	30.92	55.74	21.40	6.85	0.0033	0.0008	57.46	65.36	22.95	23.01
DiG-L [47]	102.90	10.93	0.0808	0.0050	15.95	23.63	44.79	25.23	6.70	0.0032	0.0009	54.90	62.46	19.25	23.58
PixArt- Σ -L [3]	87.43	8.68	0.0692	0.0034	18.65	27.71	51.64	22.57	7.16	0.0031	0.0011	55.46	64.86	22.27	22.45
EDiT [1]	87.08	7.76	0.0666	0.0026	19.57	26.76	50.85	23.61	7.74	0.0039	0.0014	58.02	67.44	18.28	23.39
Sana-L [41]	71.26	7.09	0.0538	0.0025	23.60	33.34	54.24	20.57	6.54	0.0045	0.0011	64.04	74.50	20.19	22.83
DyDi-LiT-L	62.63	6.80	0.0446	0.0024	26.28	35.30	55.91	20.03	6.18	0.0046	0.0008	66.65	75.43	20.41	22.85

Table 1. **Quantitative results on Sub-IN at 256×256 resolution.** Best results are in **bold**. “S”, “B”, and “L” denote the small, base, and large model sizes, respectively. “P” and “R” refer to Precision and Recall, respectively. “CFG” indicates classifier-free guidance [16] scale.

Models	CFG=1.0							CFG=4.0							GFLOPs
	FID ↓	sFID ↓	KID ↓	sKID ↓	IS ↑	P% ↑	R% ↑	FID ↓	sFID ↓	KID ↓	sKID ↓	IS ↑	P% ↑	R% ↑	
DiT-L [27]	88.17	6.37	0.0723	0.0023	19.47	26.58	54.90	22.71	6.32	0.0029	0.0010	54.00	63.93	24.02	106.42
DiG-L [47]	134.79	13.13	0.1241	0.0047	12.84	18.20	44.80	34.29	6.81	0.0067	0.0010	45.31	48.20	25.77	94.15
PixArt- Σ -L [3]	122.84	9.96	0.1065	0.0044	13.01	20.75	38.07	45.54	7.64	0.0128	0.0013	35.50	40.78	28.78	97.38
EDiT [1]	144.85	18.56	0.1082	0.0102	9.24	18.38	26.39	29.90	5.95	0.0041	0.0008	49.07	45.91	24.24	96.17
Sana-L [41]	82.30	5.73	0.0658	0.0018	21.47	28.52	56.08	21.86	6.40	0.0030	0.0011	58.09	69.43	22.12	98.46
DyDi-LiT-L	71.79	5.10	0.0542	0.0014	23.73	31.52	59.89	21.30	5.77	0.0039	0.0007	59.77	71.42	20.32	98.55

Table 2. **Quantitative results on Sub-IN at 512×512 resolution.** Best results are in **bold**.

For Sub-IN, we randomly sample 100 classes from ImageNet-1K, yielding a benchmark containing 128,982 images. On Sub-IN, all models are trained for 200 epochs (*i.e.*, 100,600 iterations) using mixed precision (BFLOAT16 and Float32) to reduce computational cost. The only exception is DiG [47], which is trained in FP32 (*i.e.*, full precision) due to numerical instability observed with mixed-precision training. All remaining settings mirror those used for ImageNet-1K.

Evaluation metrics. For ImageNet-1K benchmark, we use the official evaluation code and reference batch provided by OpenAI [5] to compute FID [15], sFID [26], Inception Score (IS) [32], Precision, and Recall [20]. Following DiT [27], we set the number of sampling steps to 250 and synthesize 50 samples per class, yielding 50K images for evaluation. For Sub-IN benchmark, we recompute the reference batch on the selected 100 classes and additionally report KID and sKID [2] to enable a more thorough comparison. Across all resolutions and model scales on Sub-IN, we use 200 sampling steps and generate 300 samples per class, yielding 30K images for evaluation.

Architecture details. For both benchmarks, the default patch size is 2. In DyDi-LiT, all learnable kernel factor scalars γ are initialized to 3, and all learnable differential factor scalars λ are initialized to 0.01. From the small to large versions, n_p is set to 3, 5, and 7, while both n_F and n_D are set to 9, 15, and 21. The number of blocks in DyDi-LiT is fixed

at 9 across all scales. DyDi-LiT follows the feedforward network structure from Sana, which has been shown to be effective. On Sub-IN benchmark, we evaluate small, base, and large variants, with hidden dimensions d set to 384, 512, and 768, respectively. In DiT [27], the number of blocks is fixed at 12 for all model sizes. For a fairer comparison, we adjust the number of blocks in other models to ensure their FLOPs roughly aligned with those of DiT.

4.2. Quantitative Results

We compare DyDi-LiT with DiT [27], DiG [47], PixArt- Σ [3], EDiT [1] and Sana [41] on Sub-IN benchmark. For ImageNet-1K benchmark, we evaluate DyDi-LiT against DiT [27], MoH-DiT [18], DiG [47] and LiT [36]. Given the strong performance of Sana [41] on Sub-IN, we additionally include it for comparison on ImageNet-1K. For further quantitative comparison results, please refer to Appendix A.

Comparisons on Sub-IN benchmark. Table 1 and Table 2 demonstrate that DyDi-LiT significantly outperforms previous efficient diffusion models across multiple metrics. Notably, while different models exhibit comparable FLOPs at the resolution of 256×256 , when using the same large-version architecture at 512×512 , DiT incurs an apparently higher per-step inference cost than other lightweight models. As shown in Fig. 1(a), this gap further widens at higher resolutions—at 2048×2048 , the inference cost of DiT is

Models	CFG=1.0					CFG=1.5					CFG=4.0				
	FID ↓	sFID ↓	IS ↑	P ↑	R ↑	FID ↓	sFID ↓	IS ↑	P ↑	R ↑	FID ↓	sFID ↓	IS ↑	P ↑	R ↑
DiT-S [27]	68.40	-	-	-	-	-	-	-	-	-	-	-	-	-	-
DiT-S* [27]	68.18	12.06	17.84	0.36	0.54	45.45	9.06	25.39	0.47	0.54	16.60	9.86	46.11	0.76	0.29
MoH-DiT-S [18]	67.25	12.15	20.52	0.37	0.58	-	-	-	-	-	-	-	-	-	-
DiG-S [47]	62.06	11.77	22.81	0.39	0.56	-	-	-	-	-	-	-	-	-	-
LiT-S [36]	63.21	-	22.08	0.39	0.58	-	-	-	-	-	-	-	-	-	-
Sana-S* [41]	64.15	12.83	19.20	0.38	0.53	41.01	9.76	27.69	0.50	0.52	15.19	9.66	48.15	0.80	0.26
DyDi-LiT-S	58.52	11.77	20.78	0.40	0.58	35.30	8.96	30.42	0.53	0.54	13.36	9.68	52.00	0.84	0.24

Table 3. Quantitative results on ImageNet-1K at 256×256 resolution. Best results are in **bold**. “-” indicates that the result has not been officially reported. “*” represents the results is replicated according to the released code.

Models	FID ↓	sFID ↓	KID ↓	sKID ↓	IS ↑	P% ↑	R% ↑
Sana-S	28.00	6.95	0.0044	0.0011	49.37	55.01	22.61
+focused kernel [12]	28.20	6.94	0.0044	0.0011	49.79	55.99	23.59
+dynamic measure kernel	27.87	7.07	0.0043	0.0011	50.08	56.49	23.40
+dynamic projection module	27.46	6.83	0.0043	0.0011	50.65	57.38	22.15
+token differential operator	26.20	6.14	0.0039	0.0009	52.21	57.73	23.91
+reparameterization	24.48	6.49	0.0033	0.0009	53.82	63.26	20.93

Table 4. Ablation on the components of DyDi-LiT. Best results are in **bold**.

several times greater than those of linear-attention models—underscoring the practical advantages of DyDiLA.

Comparisons on Imagenet-1K benchmark. Table 3 shows that DyDi-LiT surpasses prior SOTA methods across multiple metrics on the widely acknowledged benchmark, further confirming its robustness.

4.3. Qualitative Results

Comparisons on the generated results. Fig. 3 and Fig. 4 show the generation results of models with different scales at 256×256 and 512×512 resolutions, respectively. Consistent with the observations in DiT [27], smaller models sometimes fail to produce structurally coherent images, while larger models demonstrate progressively stronger generative capabilities. Overall, DyDi-LiT achieves the best results in terms of both structural coherence and visual detail. For further qualitative comparisons, please refer to Appendix B.

Visualization of the routing process in dynamic projection module. To illustrate the role of dynamic projection module in decoupling token representations, we visualize the routing results across blocks in the small version of DyDi-LiT. Specifically, for images generated with different class conditions, we visualize the projector most frequently selected by tokens in each block. As shown in Fig. 5, when generating images of different classes, each projector exhibits varying access frequencies, indicating that using dynamic projection module leads to more effectively disentangled token representations.

5. Ablation Study

In this section, we begin by evaluating the components of DyDi-LiT and analyzing their impact on the resulting attention maps. We then compare the two differential paradigms introduced in §3.2. Finally, we assess the influence of the differential factor and its initialization strategy. The default CFG scale is set to 4.0.

Ablation on the components of DyDiLA. As shown in Table 4, we take Sana [41] as our initial baseline. First, we observe that directly using the vanilla focused kernel [12] leads to performance improvements, while incorporating dynamic measure kernel further enhances the performance, indicating that dynamic measure kernel provides better similarity measurement. Next, we replace the projections of Q and K with dynamic projections, which improves model performance by facilitating the decoupled representations of tokens. Further incorporating token differential operator leads to better results by enhancing the robustness of query-to-key retrieval. The performance gains from re-parameterization may suggest the importance of feature diversity introduced by convolution operations.

Ablation on the attention maps. To intuitively illustrate the impact of each component of DyDiLA on the attention mechanism, we visualize the intermediate attention maps computed after tokens sequentially pass through each component. For a randomly selected query token, we visualize its attention weights on the key tokens, color-mapped from low (blue) to high (red). Fig. 6(a) shows that the vanilla linear attention (Sana) struggles to effectively capture the relationships between the query and key tokens. In contrast, Figs. 6(b-d) show that as tokens progressively pass through

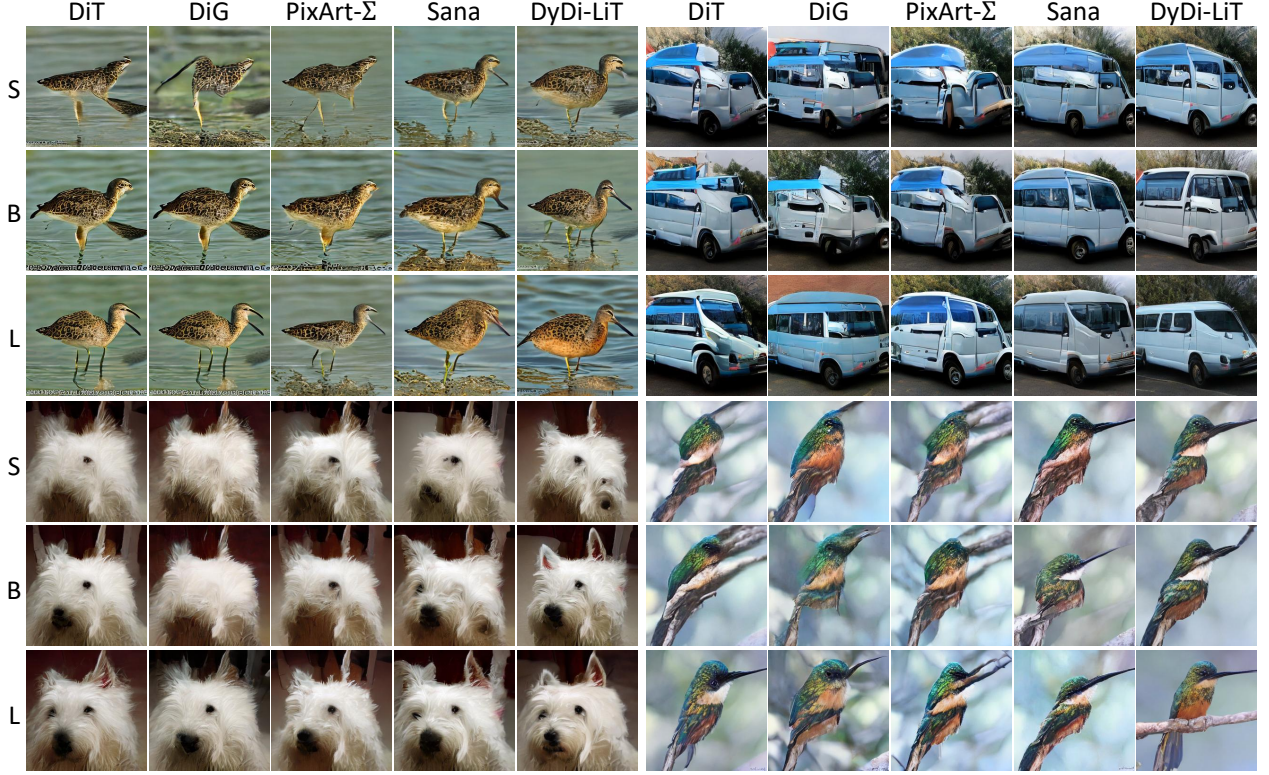


Figure 3. **Generation results of models on Sub-IN benchmark at 256×256 resolution.** CFG scale is 4.0. As the model size increases, the generation quality consistently improves. Overall, DyDi-LiT produces the highest-quality images. *Best viewed zoomed-in.*

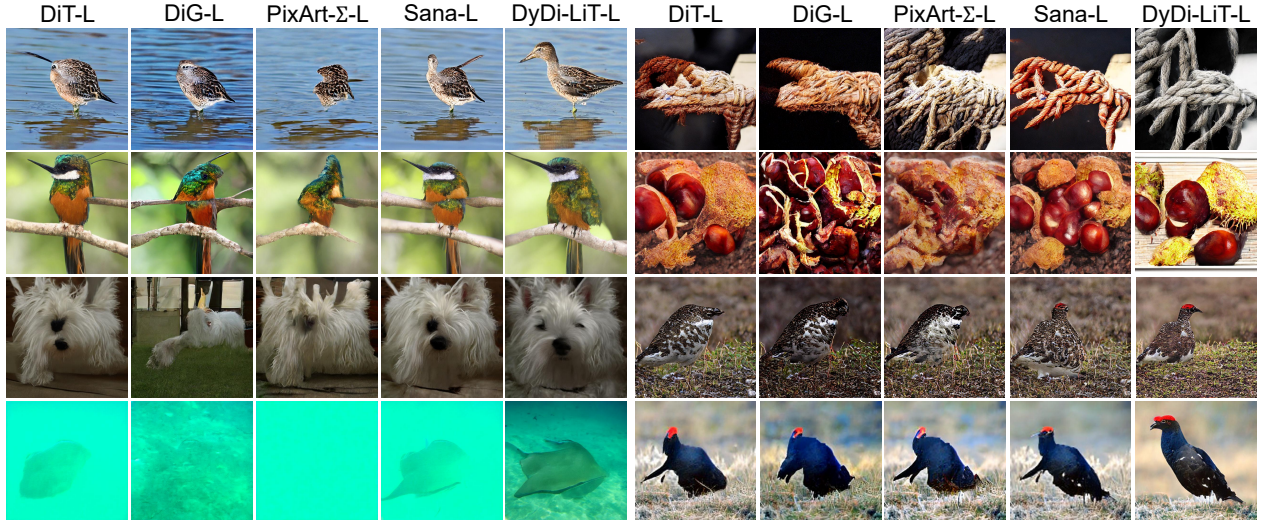


Figure 4. **Generation results of large version models on Sub-IN benchmark at 512×512 resolution.** CFG scale is 4.0. Overall, DyDi-LiT produces the highest-quality images. *Best viewed zoomed-in.*

Models	FID \downarrow	sFID \downarrow	KID \downarrow	sKID \downarrow	IS \uparrow	P% \uparrow	R% \uparrow	GFLOPS
Attention map-wise paradigm	26.62	6.75	0.0037	0.0010	51.22	59.55	21.36	6.45
Token-wise paradigm (Default)	26.20	6.14	0.0039	0.0009	52.21	57.73	23.91	5.98

Table 5. **Ablation on differential paradigms.** The best results are marked in **bold**.

Models	FID ↓	sFID ↓	KID ↓	sKID ↓	IS ↑	P% ↑	R% ↑
Increasing initialization	29.30	6.73	0.0050	0.0011	48.23	55.86	22.84
Initialization to 0.01 (Default)	26.20	6.14	0.0039	0.0009	52.21	57.73	23.91

Table 6. **Ablation on initialization methods of differential factors.** The best results are marked in **bold**.

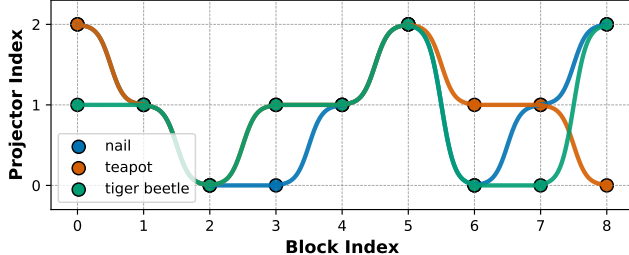


Figure 5. **Routing visualization of dynamic projection module.** For images from various categories, the most frequently accessed projector in each block is shown, revealing category-specific routing and disentangled token representations.

subsequent components, the model’s ability to represent fine-grained semantic differences between the query and keys is gradually enhanced.

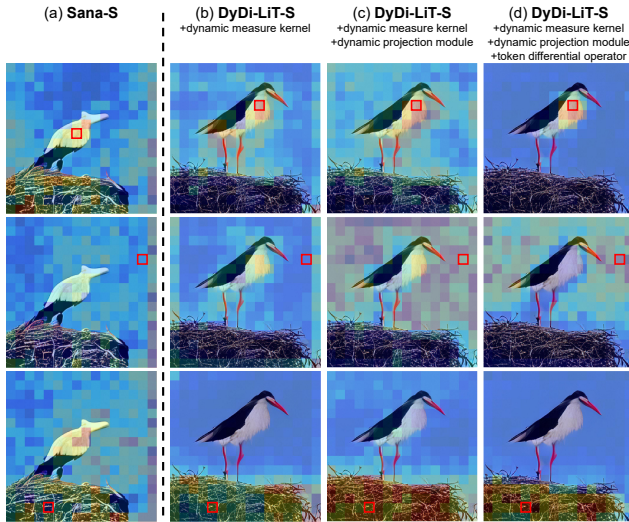


Figure 6. **Visualization of the effect of ablating each DyDiLA component on attention maps.** The red box denotes a randomly selected query token, with the corresponding key token weights shown from low (blue) to high (red).

Ablation on the differential paradigm. In this experiment, we compare the performance of token-wise and attention map-wise differential paradigm (corresponding to Eq. (9) and Eq. (10), respectively). Table 5 reveals that no significant performance difference between the two differential approaches, suggesting that the key to improving retrieval performance lies in the differential computation itself, rather than in the specific differential formula. Notably, the token-wise paradigm is computationally superior, requiring only two matrix multiplications compared to four for the attention

map-wise paradigm. This makes it significantly more efficient, especially for high-resolution image generation. We further investigate the differential factors learned through the two differential paradigms. Specifically, we compute the mean factor value at each block. As shown in Fig. 7(a), the attention map-wise paradigm produces larger differential factors compared to token-wise paradigm. Notably, a consistent trend is that the factors increase with network depth, suggesting that deeper layers need to prune more redundant information to achieve a more precise query-to-key retrieval. For further discussion on the paradigms, please refer to Appendix C.

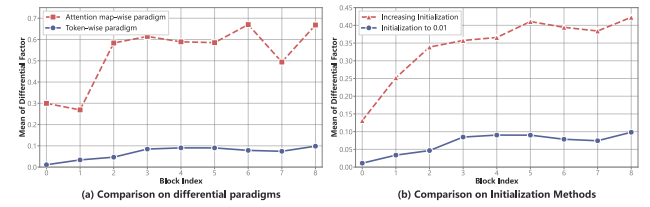


Figure 7. **Curves of differential factors varying with network depth.** (a) The attention map-wise paradigm learns differential factors with larger magnitudes. (b) Initializing with larger values in deeper layers results in significantly greater learned factors. Overall, the differential factor consistently increases with network depth.

Ablation on the initialization method of differential factors. Motivated by the observation in Fig. 7(a) that deeper layers learn larger differential factors, we explore whether an initialization strategy that explicitly mimics this trend can improve performance. Specifically, we initialize the factors to increase from 0.2 to 0.8 with network depth. Fig. 7(b) confirms that this initialization indeed results in larger learned factors. However, Table 6 indicates that this approach leads to performance degradation. We attribute this to excessive differencing, which causes a loss of critical information.

6. Conclusion

This paper introduces Dynamic Differential Linear Attention (DyDiLA) to alleviate the oversmoothing problem inherent in linear diffusion transformers, enabling high-fidelity image synthesis. Combining a dynamic projection module, a dynamic measure kernel, and a token differential operator, DyDiLA sharpens attention, preserves token diversity, and improves retrieval capability. When integrated into the LiTs baseline, DyDi-LiT retains linear complexity while matching or exceeding SOTA diffusion models across multiple metrics, thereby narrowing the gap with quadratic attention and enabling scalable, high-quality generation.

References

[1] Philipp Becker, Abhinav Mehrotra, Ruchika Chavhan, Malcolm Chadwick, Luca Morreale, Mehdi Noroozi, Alberto Gil Ramos, and Sourav Bhattacharya. EDiT: Efficient diffusion transformers with linear compressed attention. *arXiv:2503.16726*, 2025. 1, 2, 5, 11

[2] Mikołaj Bińkowski, Danica J Sutherland, Michael Arbel, and Arthur Gretton. Demystifying MMD GANs. In *ICLR*, 2018. 5

[3] Junsong Chen, Chongjian Ge, Enze Xie, Yue Wu, Lewei Yao, Xiaozhe Ren, Zhongdao Wang, Ping Luo, Huchuan Lu, and Zhenguo Li. Pixart- σ : Weak-to-strong training of diffusion transformer for 4k text-to-image generation. In *ECCV*, pages 74–91, 2024. 1, 2, 5, 11

[4] Junsong Chen, Yue Wu, Simian Luo, Enze Xie, Sayak Paul, Ping Luo, Hang Zhao, and Zhenguo Li. Pixart- δ : Fast and controllable image generation with latent consistency models. *arXiv:2401.05252*, 2024. 1

[5] Prafulla Dhariwal and Alexander Nichol. Diffusion models beat gans on image synthesis. *NIPS*, 34:8780–8794, 2021. 4, 5

[6] Kingma Diederik. Adam: A method for stochastic optimization. In *ICLR*, 2014. 4

[7] Xiaohan Ding, Yuchen Guo, Guiguang Ding, and Jungong Han. ACNet: Strengthening the kernel skeletons for powerful cnn via asymmetric convolution blocks. In *ICCV*, pages 1911–1920, 2019. 4

[8] Patrick Esser, Sumith Kulal, Andreas Blattmann, Rahim Entezari, Jonas Müller, Harry Saini, Yam Levi, Dominik Lorenz, Axel Sauer, Frederic Boesel, et al. Scaling rectified flow transformers for high-resolution image synthesis. In *ICML*, 2024. 1

[9] Zhengcong Fei, Mingyuan Fan, Changqian Yu, and Junshi Huang. Scalable diffusion models with state space backbone. *arXiv:2402.05608*, 2024. 1, 2

[10] Zhida Feng, Zhenyu Zhang, Xintong Yu, Yewei Fang, Lanxin Li, Xuyi Chen, Yuxiang Lu, Jiaxiang Liu, Weichong Yin, Shikun Feng, et al. ERNIE-ViLG 2.0: Improving text-to-image diffusion model with knowledge-enhanced mixture-of-denoising-experts. In *CVPR*, pages 10135–10145, 2023. 1

[11] Albert Gu and Tri Dao. Mamba: Linear-time sequence modeling with selective state spaces. *arXiv:2312.00752*, 2023. 2

[12] Dongchen Han, Xuran Pan, Yizeng Han, Shiji Song, and Gao Huang. Flatten transformer: Vision transformer using focused linear attention. In *ICCV*, pages 5961–5971, 2023. 1, 2, 3, 4, 6

[13] Dongchen Han, Tianzhu Ye, Yizeng Han, Zhuofan Xia, Siyuan Pan, Pengfei Wan, Shiji Song, and Gao Huang. Agent attention: On the integration of softmax and linear attention. In *ECCV*, pages 124–140, 2024. 1, 2

[14] Kaiming He, Xiangyu Zhang, Shaoqing Ren, and Jian Sun. Deep residual learning for image recognition. In *CVPR*, pages 770–778, 2016. 11

[15] Martin Heusel, Hubert Ramsauer, Thomas Unterthiner, Bernhard Nessler, and Sepp Hochreiter. GANs trained by a two time-scale update rule converge to a local nash equilibrium. *NIPS*, 30, 2017. 5

[16] Jonathan Ho and Tim Salimans. Classifier-free diffusion guidance. In *NIPS*, 2022. 5

[17] Vincent Tao Hu, Stefan Andreas Baumann, Ming Gui, Olga Grebenkova, Pingchuan Ma, Johannes Fischer, and Björn Ommer. Zigma: A dit-style zigzag mamba diffusion model. In *ECCV*, pages 148–166, 2024. 1, 2

[18] Peng Jin, Bo Zhu, Li Yuan, and Shuicheng Yan. Moh: Multi-head attention as mixture-of-head attention. *arXiv preprint arXiv:2410.11842*, 2024. 1, 2, 5, 6

[19] Diederik P Kingma, Max Welling, et al. Auto-encoding variational bayes, 2013. 2, 4

[20] Tuomas Kynkääniemi, Tero Karras, Samuli Laine, Jaakko Lehtinen, and Timo Aila. Improved precision and recall metric for assessing generative models. *NIPS*, 32, 2019. 5

[21] Songhua Liu, Weihao Yu, Zhenxiong Tan, and Xinchao Wang. Linfusion: 1 gpu, 1 minute, 16k image. *arXiv:2409.02097*, 2024. 1, 2

[22] Yixin Liu, Kai Zhang, Yuan Li, Zhiling Yan, Chujie Gao, Ruoxi Chen, Zhengqing Yuan, Yue Huang, Hanchi Sun, Jianfeng Gao, et al. Sora: A review on background, technology, limitations, and opportunities of large vision models. *arXiv:2402.17177*, 2024. 1

[23] Ilya Loshchilov and Frank Hutter. Decoupled weight decay regularization. In *ICLR*, 2019. 4

[24] Kaiyue Lu, Zexiang Liu, Jianyuan Wang, Weixuan Sun, Zhen Qin, Dong Li, Xuyang Shen, Hui Deng, Xiaodong Han, Yuchao Dai, et al. Linear video transformer with feature fixation. *arXiv:2210.08164*, 2022. 2

[25] Laurens van der Maaten and Geoffrey Hinton. Visualizing data using t-sne. *JMLR*, 9(Nov):2579–2605, 2008. 11

[26] Charlie Nash, Jacob Menick, Sander Dieleman, and Peter W Battaglia. Generating images with sparse representations. In *ICML*, 2021. 5

[27] William Peebles and Saining Xie. Scalable diffusion models with transformers. In *ICCV*, pages 4195–4205, 2023. 1, 3, 4, 5, 6, 11

[28] William Peebles and Saining Xie. Scalable diffusion models with transformers. In *ICCV*, pages 4195–4205, 2023. 2

[29] Yifan Pu, Zhuofan Xia, Jiayi Guo, Dongchen Han, Qixiu Li, Duo Li, Yuhui Yuan, Ji Li, Yizeng Han, Shiji Song, et al. Efficient diffusion transformer with step-wise dynamic attention mediators. In *ECCV*, pages 424–441, 2024. 1, 2

[30] Robin Rombach, Andreas Blattmann, Dominik Lorenz, Patrick Esser, and Björn Ommer. High-resolution image synthesis with latent diffusion models. In *CVPR*, pages 10684–10695, 2022. 4

[31] Olga Russakovsky, Jia Deng, Hao Su, Jonathan Krause, Sanjeev Satheesh, Sean Ma, Zhiheng Huang, Andrej Karpathy, Aditya Khosla, Michael Bernstein, et al. Imagenet large scale visual recognition challenge. *International journal of computer vision*, 115:211–252, 2015. 4

[32] Tim Salimans, Ian Goodfellow, Wojciech Zaremba, Vicki Cheung, Alec Radford, and Xi Chen. Improved techniques for training GANs. *NIPS*, 29, 2016. 5

[33] Zhuoran Shen, Mingyuan Zhang, Haiyu Zhao, Shuai Yi, and Hongsheng Li. Efficient attention: Attention with linear complexities. In *WACV*, pages 3531–3539, 2021. [2](#)

[34] Minglei Shi, Ziyang Yuan, Haotian Yang, Xintao Wang, Mingwu Zheng, et al. DiffMoE: Dynamic token selection for scalable diffusion transformers. *arXiv:2503.14487*, 2025. [1](#)

[35] Chenhui Wang, Tao Chen, Zhihao Chen, Zhizhong Huang, Taoran Jiang, Qi Wang, and Hongming Shan. FLDM-VTON: Faithful latent diffusion model for virtual try-on. In *IJCAI*, 2024. [1](#)

[36] Jiahao Wang, Ning Kang, Lewei Yao, Mengzhao Chen, Chengyue Wu, Songyang Zhang, Shuchen Xue, Yong Liu, Taiqiang Wu, Xihui Liu, et al. LiT: Delving into a simplified linear diffusion transformer for image generation. *arXiv:2501.12976*, 2025. [1, 2, 5, 6](#)

[37] Sinong Wang, Belinda Z Li, Madian Khabsa, Han Fang, and Hao Ma. Linformer: Self-attention with linear complexity. *arXiv:2006.04768*, 2020. [1](#)

[38] Shuai Wang, Zhi Tian, Weilin Huang, and Limin Wang. Ddt: Decoupled diffusion transformer. *arXiv:2504.05741*, 2025. [1](#)

[39] Wenhui Wang, Enze Xie, Xiang Li, Deng-Ping Fan, Kaitao Song, Ding Liang, Tong Lu, Ping Luo, and Ling Shao. Pyramid vision transformer: A versatile backbone for dense prediction without convolutions. In *CVPR*, pages 568–578, 2021. [1, 2](#)

[40] Wenhui Wang, Enze Xie, Xiang Li, Deng-Ping Fan, Kaitao Song, Ding Liang, Tong Lu, Ping Luo, and Ling Shao. Pvt v2: Improved baselines with pyramid vision transformer. *Computational visual media*, 8(3):415–424, 2022. [1, 2](#)

[41] Enze Xie, Junsong Chen, Junyu Chen, Han Cai, Haotian Tang, Yujun Lin, Zhekai Zhang, Muyang Li, Ligeng Zhu, Yao Lu, et al. SANA: Efficient high-resolution text-to-image synthesis with linear diffusion transformers. In *ICLR*, 2025. [1, 2, 5, 6, 11](#)

[42] Enze Xie, Junsong Chen, Yuyang Zhao, Jincheng Yu, Ligeng Zhu, Chengyue Wu, Yujun Lin, Zhekai Zhang, Muyang Li, Junyu Chen, et al. SANA 1.5: Efficient scaling of training-time and inference-time compute in linear diffusion transformer. In *ICML*, 2025. [1, 2](#)

[43] Zeyue Xue, Guanglu Song, Qiushan Guo, Boxiao Liu, Zhuofan Zong, Yu Liu, and Ping Luo. RAPHAEL: Text-to-image generation via large mixture of diffusion paths. *NIPS*, 36: 41693–41706, 2023. [1](#)

[44] Jing Nathan Yan, Jiatao Gu, and Alexander M Rush. Diffusion models without attention. In *CVPR*, pages 8239–8249, 2024. [1, 2](#)

[45] Tianzhu Ye, Li Dong, Yuqing Xia, Yutao Sun, Yi Zhu, Gao Huang, and Furu Wei. Differential transformer. In *ICLR*, 2025. [2, 4](#)

[46] Weihao Yu and Xinchao Wang. Mambaout: Do we really need mamba for vision? In *CVPR*, pages 4484–4496, 2025. [1, 2](#)

[47] Lianghui Zhu, Zilong Huang, Bencheng Liao, Jun Hao Liew, Hanshu Yan, Jiashi Feng, and Xinggang Wang. DiG: Scalable and efficient diffusion models with gated linear attention. In *CVPR*, pages 7664–7674, 2025. [1, 2, 5, 6, 11](#)

Models	CFG=2.0							CFG=3.0							GFLOPs
	FID ↓	sFID ↓	KID ↓	sKID ↓	IS ↑	P% ↑	R% ↑	FID ↓	sFID ↓	KID ↓	sKID ↓	IS ↑	P% ↑	R% ↑	
DiT-S [27]	65.45	7.59	0.0379	0.0023	25.88	33.41	43.74	43.52	6.68	0.0159	0.0012	36.73	42.29	34.04	6.06
DiG-S [47]	82.20	9.64	0.0502	0.0035	22.08	28.18	36.57	55.55	7.94	0.0229	0.0019	32.09	37.00	30.99	5.92
PixArt- Σ -S [3]	76.08	9.55	0.0449	0.0034	22.91	30.36	38.59	51.63	7.84	0.0204	0.0017	33.34	39.47	32.54	5.78
EDiT [1]	69.59	8.29	0.0384	0.0026	25.71	32.67	35.91	45.27	7.42	0.0157	0.0016	37.49	44.32	27.34	5.91
Sana-S [41]	53.54	7.12	0.0279	0.0021	31.68	39.18	42.52	33.30	6.44	0.0093	0.0012	43.98	51.21	33.42	5.97
DyDi-LiT-S	44.06	6.54	0.0203	0.0017	35.34	44.58	42.28	27.45	6.03	0.0059	0.0010	47.53	58.50	31.13	5.98

Table 7. Additional quantitative results on Sub-IN at 256×256 resolution. Best results are in **bold**.

Models	CFG=1.25					CFG=2.00					CFG=3.00				
	FID ↓	sFID ↓	IS ↑	P% ↑	R% ↑	FID ↓	sFID ↓	IS ↑	P% ↑	R% ↑	FID ↓	sFID ↓	IS ↑	P% ↑	R% ↑
DiT-S* [27]	55.69	10.38	21.34	41.57	54.05	31.22	7.47	32.52	56.52	48.85	19.13	7.65	41.70	69.17	37.39
Sana-S* [41]	51.41	11.16	23.49	44.05	53.29	27.36	8.12	35.00	60.60	47.24	16.75	7.89	44.02	74.53	35.34
DyDi-LiT-S	45.54	10.17	25.79	46.80	55.66	21.97	7.40	39.01	64.74	46.98	13.56	7.69	48.21	78.34	33.85

Table 8. Additional quantitative results on ImageNet-1K at 256×256 resolution. Best results are in **bold**.

Appendix

A. Additional Quantitative Comparison Results

In this section, to further validate the effectiveness of DyDi-LiT, we report additional quantitative comparisons on the Sub-IN and ImageNet-1K benchmarks using different CFG scales.

Comparisons on Sub-IN. Table 7 compare DyDi-LiT with SOTA models on Sub-IN under additional parameter settings. Consistent with the results in Table 1, DyDi-LiT surpasses the SOTA models across multiple metrics.

Comparisons on ImageNet-1K. Table 8 presents the performance of the models on the standard ImageNet-1K benchmark under different CFG scales. The overall performance trend is consistent with that in Table 3, where DyDi-LiT achieves the best results.

B. Additional Qualitative Comparison Results

Qualitative comparisons on Sub-IN. To enable a more comprehensive comparison, this section provides additional qualitative results. Fig. 8 and 9 present additional qualitative comparison results. Overall, DyDi-LiT demonstrates superior generation performance at both 265×256 and 512×512 resolutions.

Qualitative comparisons on ImageNet-1K. In this experiment, we further qualitatively compare DyDi-LiT with DiT and Sana. Fig. 10 shows that DyDi-LiT consistently outperforms other SOTA models, highlighting its application potential.

C. Further Discussion on the Token-Wise and Attention Map-Wise Differential Paradigm

In this section, we analyze the connection between the token-wise differential paradigm in Eq. (9) and the attention map-wise differential paradigm in Eq. (10). By expanding Eq. (9),

we obtain:

$$\begin{aligned}
 O &= (\tilde{Q} - \lambda^Q \tilde{Q}') \left((\tilde{K} - \lambda^K \tilde{K}')^T V \right) \\
 &= \left(\tilde{Q} \tilde{K}^T - \lambda^K \tilde{Q} \tilde{K}'^T - \lambda^Q \tilde{Q}' \tilde{K}^T + \underbrace{\lambda^Q \lambda^K \tilde{Q}' \tilde{K}'^T}_{\text{negligible}} \right) V
 \end{aligned} \tag{11}$$

Note that λ^Q and λ^K fall within the range of 0 to 0.1 (as shown in Fig. 7(a) and (b), blue lines), making the last term in Eq. (11) negligible compared to the first three terms. As a result, the token-wise differential paradigm can be approximated as a specific form of attention map-wise differential paradigm.

D. t-SNE Visualizations

To intuitively assess the models’ generation quality, we compare their t-SNE [25] visualizations. Specifically, we encode the images generated on the ImageNet-1K benchmark using a pretrained ResNet-152 [14] and apply t-SNE to the yielding embeddings. As shown in Fig. 11(a), when we randomly select several classes for t-SNE visualization, all models are able to separate class clusters. However, Fig. 11(b) shows that when we choose classes that are highly semantically similar (e.g., all strongly related to “cats”), DiT and Sana struggle to distinguish these clusters, whereas DyDi-LiT still maintains clear decision boundaries. We attribute this to DyDi-LiT’s superior attention mechanism, which allows the model to better capture subtle feature differences among closely related classes during image generation.

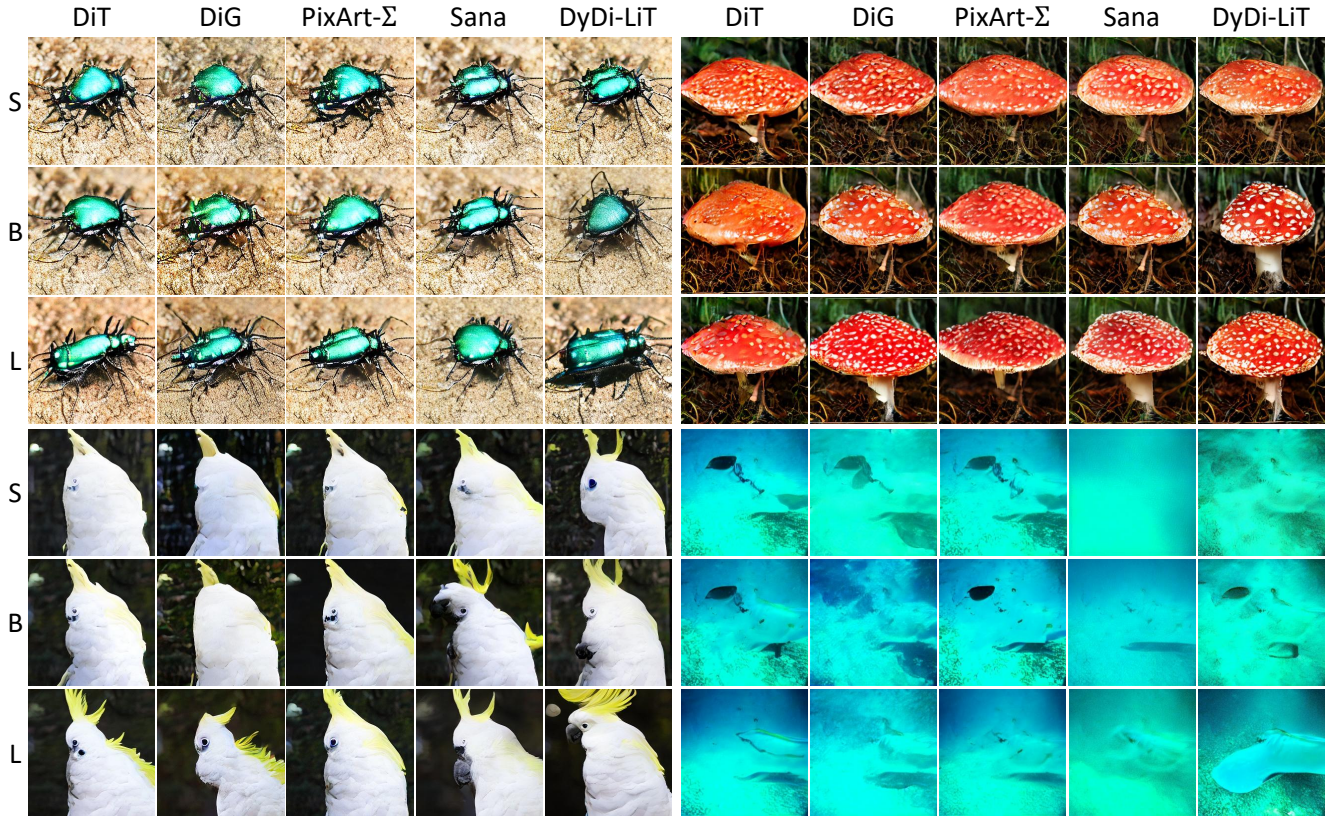


Figure 8. **Generation results of models on Sub-IN benchmark at 256×256 resolution.** CFG scale is 4.0. As the model size increases, the generation quality consistently improves. Overall, DyDi-LiT produces the highest-quality images. *Best viewed zoomed-in.*

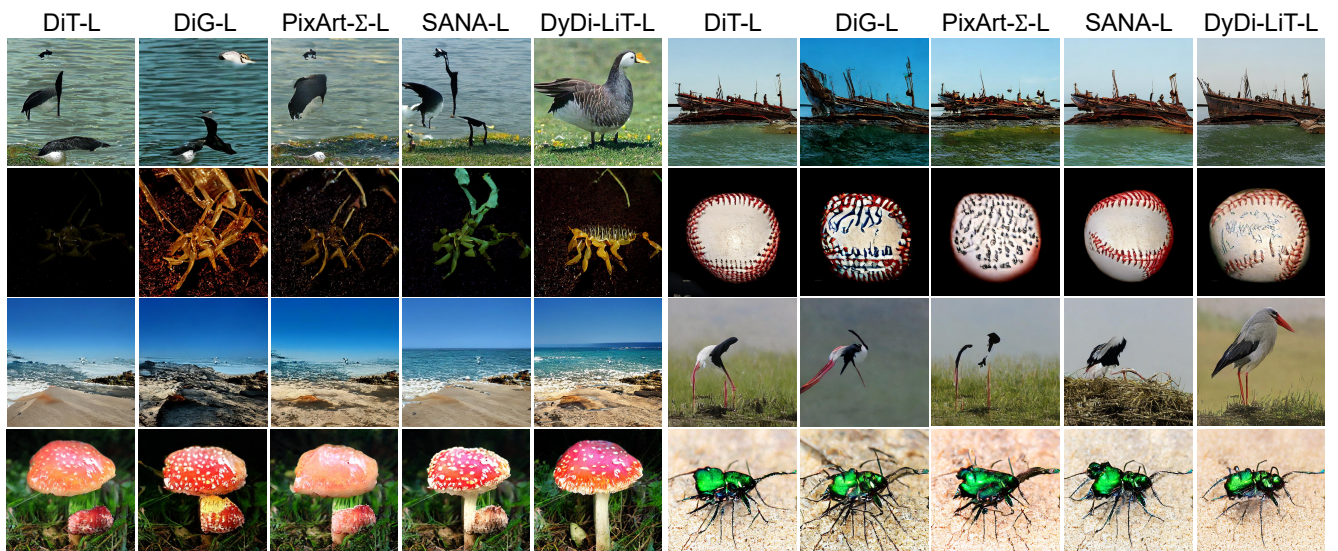


Figure 9. **Generation results of large version models on Sub-IN benchmark at 512×512 resolution.** CFG scale is 4.0. As the model size increases, the generation quality consistently improves. Overall, DyDi-LiT produces the highest-quality images. *Best viewed zoomed-in.*

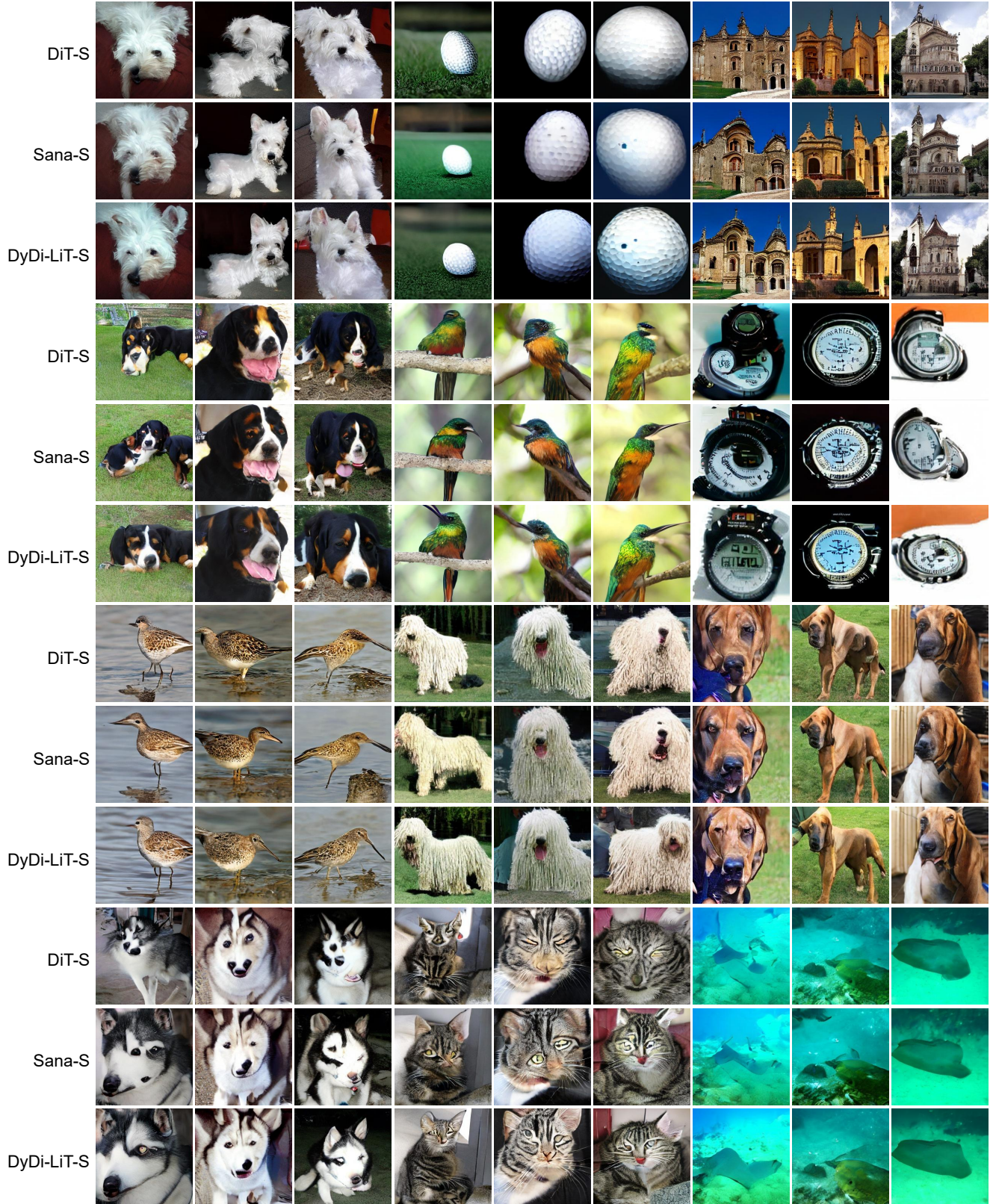
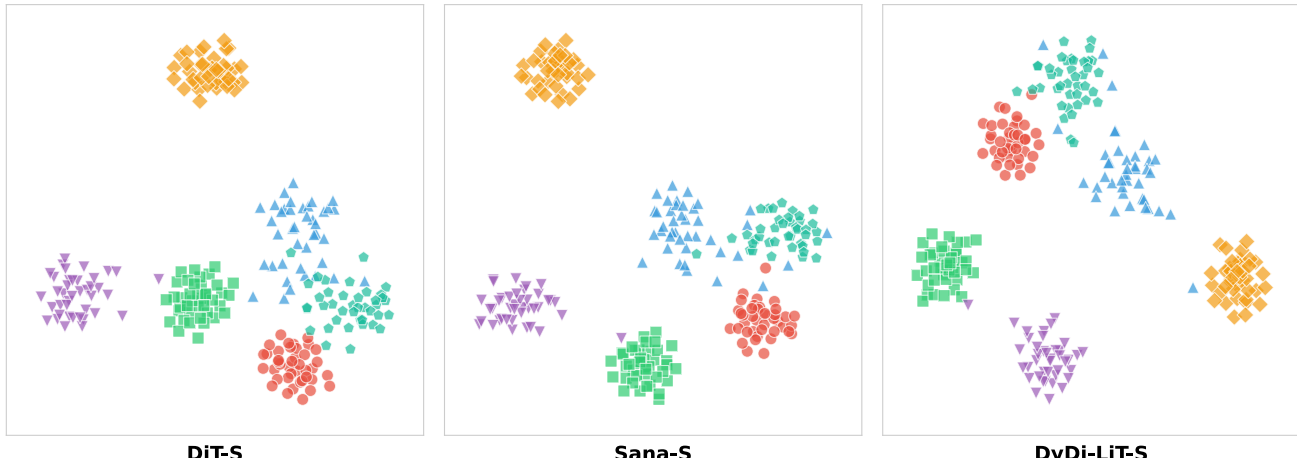
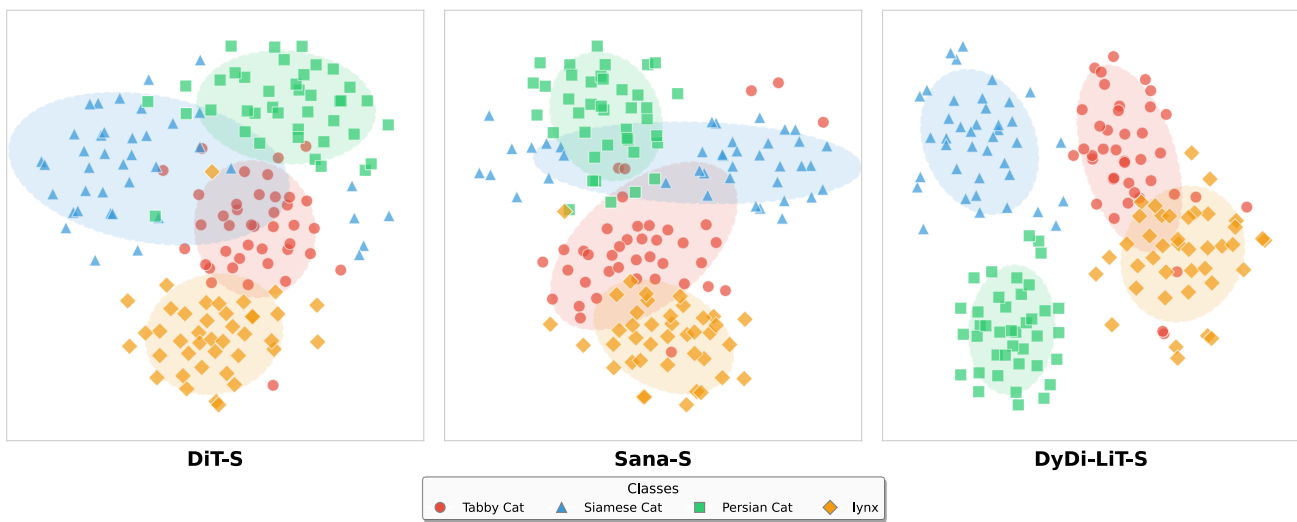


Figure 10. **Generation results of models on ImageNet-1K benchmark at 256×256 resolution.** CFG scale is 4.0. Overall, DyDi-LiT produces the highest-quality images. *Best viewed zoomed-in.*



(a) t-SNE visualization of random sampled classes



(b) t-SNE visualization of highly semantically related classes

Figure 11. **t-SNE visualizations.** (a) With randomly selected classes exhibiting clear semantic differences, all models form well-separated clusters. (b) For conceptually similar classes, DiT and Sana struggle to produce clear boundaries, whereas DyDi-LiT maintains well-defined clusters.